



# Luminosity Outburst Energized by the Collision between the Infalling Streamer and Disk in W51 North

Yan-Kun Zhang<sup>1</sup> , Xi Chen<sup>1,2</sup> , Shi-Ming Song<sup>1</sup> , and You-Xin Wang<sup>1</sup> <sup>1</sup> Center for Astrophysics, Guangzhou University, Guangzhou 510006, People's Republic of China; [chenxi@gzhu.edu.cn](mailto:chenxi@gzhu.edu.cn)<sup>2</sup> Shanghai Astronomical Observatory, Chinese Academy of Sciences, 80 Nandan Road, Shanghai 200030, People's Republic of China

Received 2023 March 4; revised 2023 May 12; accepted 2023 May 22; published 2023 June 22

## Abstract

We report the detection of the disk/torus, outflow, and inflow structures traced by H<sub>2</sub>O masers toward a high-mass young stellar object W51 North during its H<sub>2</sub>O maser outburst stage using the Karl G. Jansky Very Large Array (VLA). It is found that the disk has a radius of  $\sim 4000$  au and an inclination angle with respect to the sky plane of  $\sim 60^\circ$  by combining the VLA and the Atacama Large Millimeter/submillimeter Array data. Additionally, a peculiar flow perpendicular to the SiO bipolar outflow is detected in the H<sub>2</sub>O maser, SiO, and HC<sub>3</sub>N lines, which is newly-identified as an infalling streamer rather than an old outflow from this source, as reported in previous studies. Combining the VLA map and the Tianma radio telescope monitoring of the H<sub>2</sub>O masers suggests that the origin of the luminosity outburst of H<sub>2</sub>O masers during 2020 January–April is likely related to the energy release from the collision between the infalling streamer and the disk. This may provide an additional mechanism to account for the luminosity outburst or episodic accretion beyond disk fragmentation caused by gravitational instability.

*Unified Astronomy Thesaurus concepts:* Star formation (1569); Interstellar masers (846); Astrophysical masers (103); Young stellar objects (1834); Protostars (1302); Stellar accretion disks (1579)

## 1. Introduction

Episodic accretion is nowadays a popular topic in the research of high-mass star formation. It was first proposed by Kenyon et al. (1990) to solve the “luminosity problem” in the classical isolated steady core accretion model for low-mass star formation, where the accretion rates derived from the observed bolometric luminosity are 10–100 times lower than the values that are expected from the model (Valdivia-Mena et al. 2022). The most extremely episodic accretion events in low-mass young stellar objects (YSOs) are FUor and EXor outbursts (Herbig 1989). For FUor outbursts, the luminosity will rise about 4–6 mag (Semkov et al. 2021). For EXor outbursts, they will experience a luminosity outburst of 2–3 mag (Herbig 1977). Currently, some simulations for high-mass star formation have suggested that the accretion disk surrounding the protostar(s) in gravitational instability will be fragmented (Oliva & Kuiper 2020), which results in an increment of accretion rate, and thus luminous outbursts in high-mass star-forming regions (HMSFRs; Meyer et al. 2021). Moreover, the episodic accretion of high-mass star formation will also influence their evolution track in the Hertzsprung–Russell diagram (Meyer et al. 2019).

Diagnostic tools in radio, (sub-)millimeter, and infrared bands are generally used to observe luminosity outbursts (or episodic accretion) in HMSFRs. Traced with the 6.7 GHz class II methanol maser variability, luminosity outbursts that happened in several HMSFRs, such as S255IR-NIR3 (Stecklum et al. 2016; Caratti o Garatti et al. 2017), NGC6334I-MM1 (MacLeod et al. 2018), G358.93-0.03-MM1 (MacLeod et al. 2019; Burns et al. 2020; Miao et al. 2022), and

G24.33 + 0.14 (Hirota et al. 2022), have been detected and considered as episodic accretion events. Regarding the (sub-)millimeter and infrared bands, their luminosity outbursts have also been detected toward these accretion burst sources (e.g., Hunter et al. 2017; Caratti o Garatti et al. 2017; Brogan et al. 2019; Stecklum et al. 2021; Hunter et al. 2021). In addition, evidence of gravitational instability leading to accretion disk fragmentation was also found in G358.93-0.03 by the Karl G. Jansky Very Large Array (VLA) images of the <sup>13</sup>CH<sub>3</sub>OH, HDO, and HNCO masers (Chen et al. 2020b).

Recently, Zhang et al. (2022) used the Tianma 65 m radio telescope (TMRT) to monitor the maser and thermal line variability toward a high-mass star-forming region, W51-IRS2, which is located at a distance of 5.1 kpc (Xu et al. 2009), from January to April in 2020. This single-dish monitoring found clear variations in the spectral profiles and flux densities of the H<sub>2</sub>O, NH<sub>3</sub>, and CH<sub>3</sub>OH maser emissions, which suggests that a luminosity outburst happened in this region. With rotation diagram analysis for both NH<sub>3</sub> and CH<sub>3</sub>OH, it is derived that the temperatures from the transitions that originated from more inner layers of the molecular core generally decreased over the whole monitoring period, while those from the outer layers first increased from 2020 January 8 to April 1 and then rapidly decreased from April 1 to 7. It can be proposed that an inside-out heatwave propagation was involved with the accretion burst over a short duration (only on the order of months) and caused the drastic variability behaviors of different line transitions (see Zhang et al. 2022 for details). However, given that two highly obscured high-mass YSOs called W51 North and W51 d2 reside in the cluster environment of this source (Sollins et al. 2004; Zapata et al. 2008), we cannot determine which one is the driving object for the luminosity outburst. To figure out the origin and the physics mechanism of this outburst, we made the VLA observation for the H<sub>2</sub>O maser toward W51-IRS2 on 2020 March 31.



Original content from this work may be used under the terms of the [Creative Commons Attribution 4.0 licence](https://creativecommons.org/licenses/by/4.0/). Any further distribution of this work must maintain attribution to the author(s) and the title of the work, journal citation and DOI.

In this letter, combining the VLA and previous Atacama Large Millimeter/submillimeter Array (ALMA) observations, we report the detection of a disk (or torus) and infalling streamer around W51 North, and reveal that the origin of the luminosity outburst was likely energized by the collision between the infalling streamer and the disk.

## 2. Observation and Data Reduction

### 2.1. VLA Observation

The VLA K-band observation configured in C-array toward W51-IRS2 (J2000 position:  $19^{\text{h}}23^{\text{m}}40^{\text{s}}.047$ ,  $+14^{\circ}31'05''.530$ ) was conducted on 2020 March 31. In each cycle of about 4 minutes, the calibrator J1924+1540 (J2000 position:  $19^{\text{h}}24^{\text{m}}39^{\text{s}}.456$ ,  $+15^{\circ}40'43''.941$ ) was observed for 1 minute along with the target for gain/phase calibrating. For bandpass and flux density calibrating, the quasar 3C48 was observed. To detect the  $\text{H}_2\text{O}$ ,  $\text{NH}_3$ , and  $\text{CH}_3\text{OH}$  maser or quasi-thermal emissions, 29 narrow spectral windows (SPWs) mainly with bandwidths of 2 or 4 MHz were employed. In addition, 21 wide SPWs with a bandwidth of 128 MHz were configured to cover the continuum at the K-band (18–26.5 GHz). The SPW to cover the 22.235 GHz water maser transition has a frequency resolution of 7.812 kHz per channel, corresponding to a velocity resolution of  $\sim 0.11 \text{ km s}^{-1}$ . The other lines were observed at a velocity resolution of  $\sim 0.06 \text{ km s}^{-1}$ . To reduce the visibility data, the standard VLA Calibration Pipeline and the Common Astronomy Software Applications (CASA) package were adopted. The MIRIAD package was used to carry out image analysis. The synthesized beam size is  $1''.71 \times 1''.29$  at 22 GHz. The typical detection limit (at  $3\sigma_{\text{rms}}$ ) in a single channel is  $\sim 0.01 \text{ Jy beam}^{-1}$  at narrow SPWs. To get the positions and flux densities of the maser spots, we used the SAD command in Astronomical Image Processing System to conduct two-dimensional Gaussian fittings to each channel map of the detected maser emissions. The positions were fitted with uncertainties of smaller than  $0''.01$ . Notably, the positional uncertainty of the calibrator contributes to the absolute position uncertainty of the target, which is less than  $0''.02$  in our VLA observation.

### 2.2. ALMA Observations

To get a comprehensive understanding of the target W51-IRS2, we utilized ALMA data sets from two projects: 2013.1.00308.S and 2015.1.01596.S. The projects were both carried out in 1.3 mm, but with different angular resolutions.

#### 2.2.1. High Angular Resolution Observation

As shown in Goddi et al. (2020) and Tang et al. (2022), the high angular resolution observations at Band 6 (216–237 GHz) were conducted from 2015 October 27 to 31 as part of the ALMA Cycle 3 program 2015.1.01596.S. The baselines range from 85 to 16196 m. The synthesized beam size is  $0''.031 \times 0''.025$ . Seven SPWs with a bandwidth of  $\sim 234 \text{ MHz}$  and a spectral resolution of 564 kHz (corresponding to a velocity resolution of  $\sim 0.75 \text{ km s}^{-1}$ ) are configured for line observations. Two SPWs with a bandwidth of 1.8 GHz are used to cover the continuum emission. Data for the SiO  $J=5-4$  and  $\text{HC}_3\text{N } J=24-23$  lines and the 1.3 mm continuum emission from this observation were re-analyzed in this work. We adopted the pipeline-reduced image fits from

the archive and re-analyzed these image fits with the CASA package.

#### 2.2.2. Low Angular Resolution Observation

As shown in Ginsburg et al. (2017), the low angular resolution observations at Band 6 (218–235 GHz) were conducted in 2015 April as part of the ALMA Cycle 2 program 2013.1.00308.S. With the 12 m array used, the angular resolution was achieved to be  $0''.2$ . The 7 m Atacama Compact Array was also used, achieving an angular resolution of  $\sim 5''.3$  and a maximum spatial covering scale of  $\sim 32''$ . Data for the  $\text{C}^{18}\text{O } J=2-1$  and  $^{13}\text{CS } J=5-4$  lines achieved from this observation were used in this work. For convenience, we downloaded the image fits published in Ginsburg et al. (2017) and carried out analysis using the CASA package.

## 3. Overall Structures of W51 North

### 3.1. An Overview of the $\text{H}_2\text{O}$ Maser Spots

In the left-hand panel of Figure 1, the  $\text{H}_2\text{O}$  maser spots detected toward W51 North from our VLA observation and from Imai et al. (2002) are superposed on the outflow and possible infalling streamer (see Section 3.3) traced by the SiO line, as well as the 1.3 mm continuum emission detected by ALMA. Notably, we averaged the flux densities of the  $\text{H}_2\text{O}$  maser spots detected in the multi-epoch observations of Imai et al. (2002) for convenience to compare. The major part of the continuum emission from W51 North is at the center of the collimated and extending SiO bipolar outflow along northwest (NW) to southeast (SE), suggesting ongoing star formation in the source. Compared with previous  $\text{H}_2\text{O}$  maser spots detected by Imai et al. (2002), it can be found that more  $\text{H}_2\text{O}$  maser spots are detected by our VLA observation, particularly for those along the outflow/jet and the ring-like structures. To make a clearer comparison, we indicate the zoomed-in view of the  $\text{H}_2\text{O}$  maser distributions obtained in the two observations in the right-hand panel of Figure 1. It is clear that majority of the  $\text{H}_2\text{O}$  maser spots are located at the SE and NW subclusters, and the blue- and red-shifted (relative to the local standard of rest (LSR) systemic velocity  $V_{\text{LSR}} = \sim 60 \text{ km s}^{-1}$ )  $\text{H}_2\text{O}$  maser spots are mainly distributed around the tails of the SiO outflow. Notably, the overall orientation of the  $\text{H}_2\text{O}$  maser shows an offset of  $\sim 15^\circ$  from the SiO outflow. In addition, the strongest maser spots with velocities of about 60 and  $63 \text{ km s}^{-1}$  in our detection are distributed toward the regions associated with the infalling streamer (see Section 4 for details).

### 3.2. The Disk/Torus

The ring-like distribution of water maser spots around W51 North in the direction along northeast (NE) to southwest (SW) shown in Figure 1 may trace a Keplerian disk or torus around the protostar in W51 North. Zapata et al. (2009) detected a dusty disk with a radius of about 3000 au in the central region and a molecular ring traced by the  $\text{SO}_2$  ( $22_{2,20} \rightarrow 22_{1,21}$ ) transition with the outer radius extending to 6000 au along NE-SW from their VLA and SMA observations. Their modeling of a Keplerian infalling disk determined that the central protostar has a mass of greater than  $60 M_{\odot}$ . Furthermore, a peanut-like object with a mass of  $\sim 5 M_{\odot}$  was derived from the predominant structure of the ALMA 1.3 mm continuum shown in Figure 1, whereas the larger surrounding object has a mass of

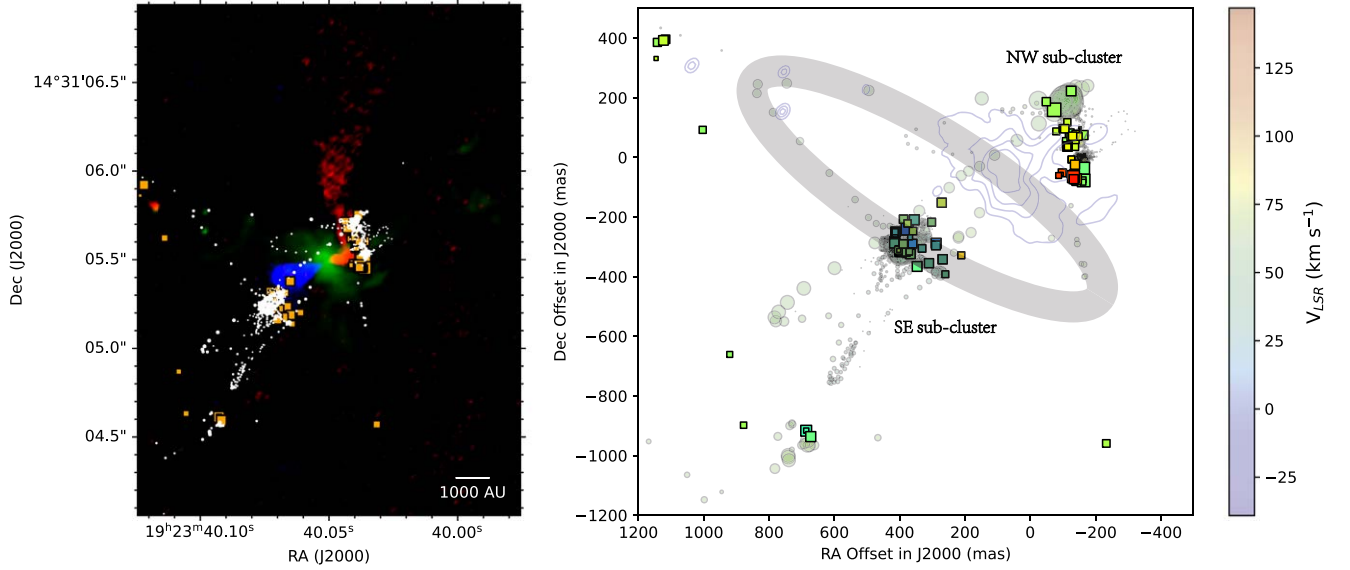


**Figure 1.** Left-hand panel: the 22.235 GHz  $\text{H}_2\text{O}$  maser spots detected toward W51 North with the VLA are shown with white circles, whereas those detected in Imai et al. (2002) using J-Net telescopes are shown with orange squares. In the background, the possible infall and the outflow traced by the  $\text{SiO } J = 5 - 4$  line detected with the ALMA are shown in red and blue, corresponding to the velocity ranges of  $67 \sim 132$  and  $-19 \sim 46 \text{ km s}^{-1}$ , respectively. The 1.3 mm continuum is shown in green. Right-hand panel: the zoomed-in view of the  $\text{H}_2\text{O}$  maser spots detected in our VLA observations and those in Imai et al. (2002), which are shown with light-colored circles and dark-colored squares, respectively. The reference position in J2000 coordinate is R.A. =  $19^{\text{h}}23^{\text{m}}40^{\text{s}}.047$ , decl. =  $+14^{\circ}31'05''.530$ . The areas of the circles or squares are proportional to the flux density of maser spots on a logarithmic scale and their colors indicate the velocity with respect to the LSR. The dark blue contours showed the 1.3 mm continuum, with the starting, step, and end level to be 0.0025, 0.0025, and  $0.0100 \text{ Jy beam}^{-1}$ . The ring-like distributed maser spots are indicated by a thick-gray elliptical ring.

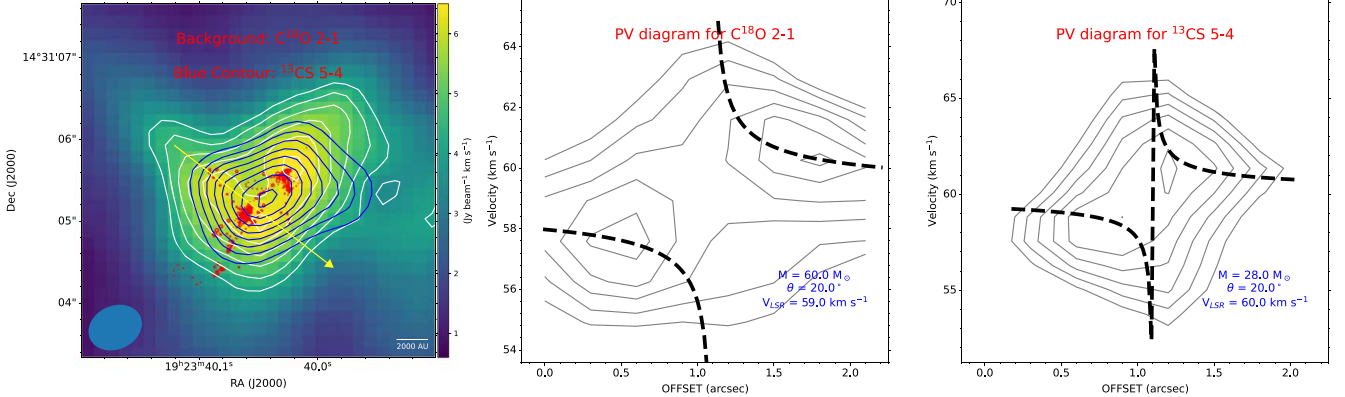


**Figure 2.** The integrated intensity maps and the P-V diagrams of the  $\text{C}^{18}\text{O } J = 2 - 1$  and  $^{13}\text{CS } J = 5 - 4$  lines observed toward W51 North with the ALMA. The left-hand panel presents the integrated intensity maps, with the starting, step, and end levels of the white/blue contours are  $4.5/4.5, 0.5/1.5,$  and  $6.5/15.0 \text{ Jy beam}^{-1} \text{ km}^{-1}$  for the  $\text{C}^{18}\text{O}/^{13}\text{CS}$  lines. The background is the  $\text{C}^{18}\text{O}$  integrated intensity map. The red points indicate the  $\text{H}_2\text{O}$  maser spots detected by the VLA observations, and the yellow arrow shows the same orientation as the major axis of the ring-like structure of the  $\text{H}_2\text{O}$  maser spots. The middle and right-hand panels present the P-V diagrams along the yellow arrow direction shown in the left-hand panel, with contour levels starting from 50% in a step of 10% of their peaks ( $0.7$  and  $1.0 \text{ Jy beam}^{-1}$  for the  $\text{C}^{18}\text{O}$  and  $^{13}\text{CS}$  lines, respectively). The best Kepler rotation models are shown by the dashed curves and are described in Appendix A.

$\sim 14 M_{\odot}$  at  $T_d \sim 390 \text{ K}$  and  $\sim 28 M_{\odot}$  at  $T_d \sim 200 \text{ K}$ , assuming that the dust emission is optically thin (Goddi et al. 2020).

To test our speculation that there may exist a Keplerian disk or torus in W51 North, we overlaid the  $\text{H}_2\text{O}$  maser spots on the  $\text{C}^{18}\text{O } J = 2 - 1$  and  $^{13}\text{CS } J = 5 - 4$  integrated intensity maps (see the left-hand panel of Figure 2), and conducted the position–velocity (P-V) diagram analysis for both lines along the possible radial direction of the disk indicated by the ring-like distributed  $\text{H}_2\text{O}$  maser spots. From this figure, it can be seen that the  $^{13}\text{CS}$  line has a more compact structure when compared to the  $\text{C}^{18}\text{O}$  line. The P-V diagrams shown in the middle and right-hand panels of Figure 2 further reveal that the P-V contours of the  $^{13}\text{CS}$  are tighter and closer to the center than those of the  $\text{C}^{18}\text{O}$  line. The profiles of their P-V diagrams

suggest that there is a Keplerian disk in the target. Utilizing the results of Zapata et al. (2009) and Goddi et al. (2020), we estimate the incline angle between the Keplerian disk plane (traced by the  $^{13}\text{CS}$  and  $\text{C}^{18}\text{O}$  lines) and the sky plane to be  $\sim 20^{\circ}$ , assuming that the masses of objects traced by  $\text{C}^{18}\text{O}$  and  $^{13}\text{CS}$  are  $60$  and  $28 M_{\odot}$ , respectively (see Appendix A for details).

It is worth noting that the distribution of the  $\text{H}_2\text{O}$  maser spots detected in our VLA observation is closer to the center than that of the  $\text{C}^{18}\text{O}$  and  $^{13}\text{CS}$  lines. In Appendix C and Figure C1, we further investigated the accretion disk traced by  $\text{H}_2\text{O}$  maser spots in 2D spaces. By analyzing the maser velocities, we found that the ring-like distribution of  $\text{H}_2\text{O}$  maser spots also traces the rotational disk in a direction that is consistent with



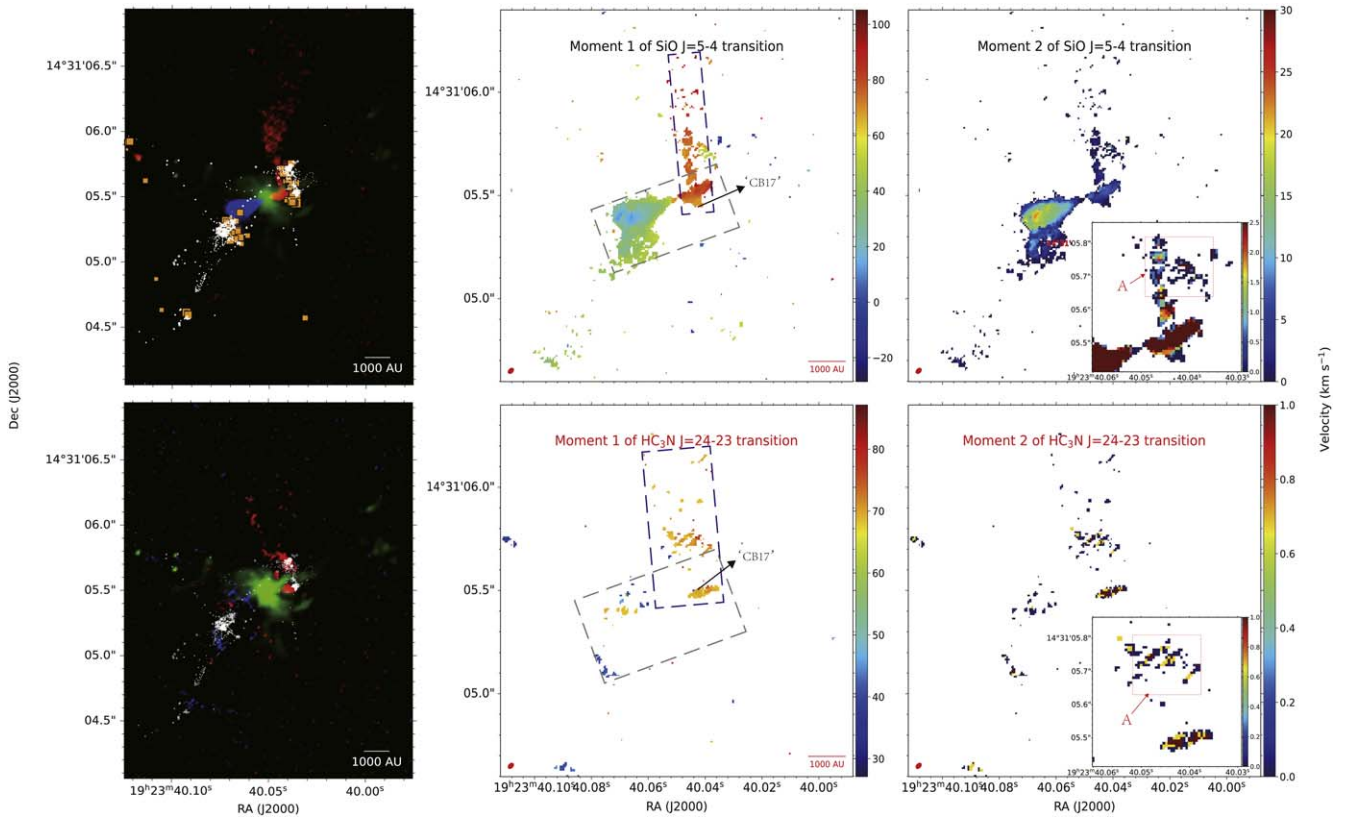


**Figure 3.** The integrated intensity (left-hand panels), velocity distribution (middle panels) and velocity dispersion (right-hand panels) maps of the SiO  $J = 5 - 4$  (upper) and HC<sub>3</sub>N  $J = 24 - 23$  (lower) for the outflow and the infalling streamer detected toward W51 North with the ALMA. In the two left-hand panels, the 1.3 mm continuum is shown in green and the H<sub>2</sub>O maser spots are shown with light white circles. The LSR velocity ranges for the red- and blue-shifted SiO components are 67–97 and -36–56 km s<sup>-1</sup>, and those for HC<sub>3</sub>N are 68–82 and 35–51 km s<sup>-1</sup>, respectively. In the velocity distribution maps, the outflow and the infalling streamer are denoted with gray and blue boxes, respectively. The arrow shows the position of the mm continuum component ‘CB17’ detected in Tang et al. (2022). Zoomed versions of the infalling streamer are shown in the right-hand corner of the velocity dispersion maps, with the A region in Figure 5 being denoted with red boxes.

the model established by Zapata et al. (2009; see Appendix Figure C1 for comparison). Since the scale of the maser ring is similar to that of the resolved W51 North detected in the ALMA observation of Goddi et al. (2020), we assumed that the mass of the central protostar is  $28 M_{\odot}$ . It is then obtained that the radius of the disk is about 4000 au and the incline angle of the disk plane traced by H<sub>2</sub>O maser spots relative to the sky plane to be  $\sim 60^{\circ}$  (see Appendix C for details). This is different from the results in Zapata et al. (2009), whose VLA and SMA observations un-resolving W51 North showed that the inner dusty disk is about 3000 au and the inclination angle with respect to the sky plane is  $\leq 30^{\circ}$  (such as the inclination from our models for the C<sup>18</sup>O and <sup>13</sup>CS lines detected in ALMA observations with lower resolutions, which also did not resolve W51 North; see above). Other than the resolution, incomplete coverage of the entire rotational disk by the water maser sampling may also explain the differences in the disk’s scale and inclination. Additionally, discrepancies between our fitting approach for the ring-shaped H<sub>2</sub>O masers, and the observations and models for SO<sub>2</sub> and dust detections in Zapata et al. (2009) could contribute to these differences. Alternatively, it could be a validation or evidence for the model of the multi-layer rotating Keplerian disk proposed by Zapata et al. (2010). In addition, no ring-like distribution of the H<sub>2</sub>O maser was found within 4000 au range. This agrees with the findings in Goddi et al. (2020) that no significant infalling and rotation features were detected in the 150–2000 au range surrounding the protostar. Tang et al. (2022) noted that fragmentation at

different levels has likely occurred in W51 North, but no formed binary or multiple star systems have been detected.

### 3.3. The Infalling Streamer

In the left-hand panel of Figure 1, a peculiarly long dragged flow traced by some H<sub>2</sub>O maser spots and the SiO  $J = 5 - 4$  transition is detected nearly perpendicular to the SiO bipolar outflow in the NW side. We inferred this to be an infalling streamer (as mentioned above) rather than an old outflow suggested by Goddi et al. (2020) according to the following analysis.

In the upper panels of Figure 3, the velocity distribution map (i.e., Moment 1) of the SiO line shows that the velocity range of the infalling streamer is 67–76 km s<sup>-1</sup>, which is slower than that of the NW red-shifted outflow (in 73–97 km s<sup>-1</sup>). In addition, the corresponding velocity dispersion map (i.e., Moment 2) of the SiO line suggests that the infalling streamer has smaller velocity dispersion in a range of 0.1–6.5 km s<sup>-1</sup>, compared to that of 4.0–8.5 km s<sup>-1</sup> in the NW red-shifted outflow. Notably, it looks from both the maps that the infalling streamer possibly intersects with the red-shifted outflow, and thus it is distinct from the red-shifted outflow.

In addition to the SiO line, we found that the HC<sub>3</sub>N  $J = 24 - 23$  line also likely traces the infalling streamer. The integrated flux density map for the red- and blue-shifted components (within LSR velocity ranges of 68–82 and 35–51 km s<sup>-1</sup>) of this line is shown in the lower left-hand panel of Figure 3. The H<sub>2</sub>O maser spots

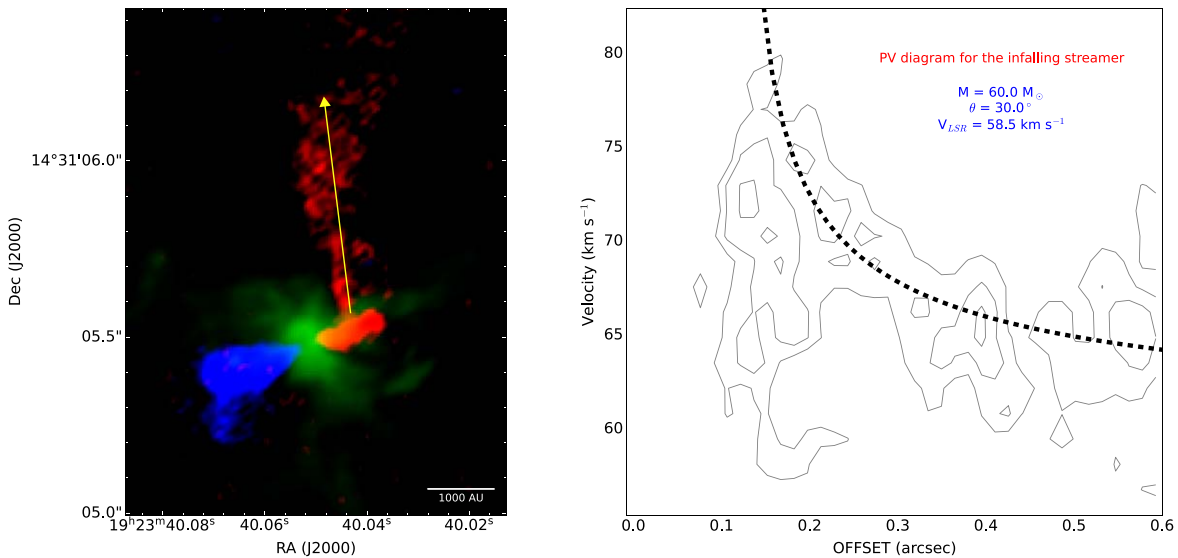


**Figure 4.** Left-hand panel: same as the left-hand panel of Figure 1 for the outflow and infalling streamer traced by the SiO detected toward W51 North with the ALMA. Right-hand panel: the P-V diagram for the infalling streamer along the arrow direction shown in the left-hand panel. The contour levels in the P-V diagram start from 50% in steps of 25% of its peak ( $0.001 \text{ Jy beam}^{-1}$  for the SiO infalling streamer). The best kinematic model for the gravitationally controlled infalling streamer is shown with the dashed curve and is described in Appendix B.

detected with the VLA were also overlaid on this sub-figure. As shown in the other two lower panels of Figure 3, regarding the velocity distribution and dispersion for the  $\text{HC}_3\text{N}$ , a significant emission along the peculiar flow was detected from the  $\text{HC}_3\text{N}$ . Notably,  $\text{HC}_3\text{N}$  as the chemically fresh molecule was thought to be an indicator of the infalling streamer in low-mass YSO Per-emb-2 (Pineda et al. 2020) and high-mass YSO G352.63-1.07 (Chen et al. 2021). Thus, its detection in W51 North enables us to infer the peculiar flow to be associated with an infalling streamer. Compared with the upper panels of Figure 3, we noticed that the distributions of the  $\text{HC}_3\text{N}$  red-shifted emission are more spatially coincident with the  $\text{H}_2\text{O}$  maser spots in the NW cluster than the SiO line. This further suggests that the maser spots in the NW cluster are likely associated with the infalling streamer, and are possibly produced by the collision between the infalling streamer and either a rotational disk or a red-shifted outflow region.

Figure 4 shows the P-V diagram along the direction of the infalling streamer traced by the SiO emission. It is clear that majority of the P-V distributions in the positional offsets from  $0''.15$  to  $0''.60$  show a classical diagram for the gravitational inflow kinematics around a central protostar, with the velocities decreasing from the location near the disk or outflow to the outer portion of the flow. This provides further evidence to support our inference that the peculiar flow is indeed an infalling streamer. With the gravitationally controlled infall model in Appendix B, we further determine that the incline angle of the infalling streamer along the line of sight (LOS) to be  $30^\circ$ , assuming the total mass in the center of the gravitational field to be  $\sim 60 M_\odot$ .

#### 4. Discussion: The Origin of the Recent Luminosity Outburst

We previously reported a three-month monitoring of the luminosity outburst traced by the  $\text{H}_2\text{O}$ ,  $\text{NH}_3$ , and  $\text{CH}_3\text{OH}$  maser and quasi-thermal emissions with the TMRT toward W51-IRS2 from 2020 January to April, and interpreted it as an inside-out heatwave propagation that was induced by a

luminosity outburst over a short duration (Zhang et al. 2022). Compared with the new VLA map of the  $\text{H}_2\text{O}$  masers during the outburst stage (on 2020 March 31) reported in this work, we can further explore the possible origins of the luminosity outburst and the variations of the interstellar environments in W51-IRS2.

In the left-hand panel of Figure 5, the  $\text{H}_2\text{O}$  maser spectra taken in the former three-month TMRT monitoring toward the target are presented. Meanwhile, the VLA  $\text{H}_2\text{O}$  maser spectrum taken on 2020 March 31 is shown in the upper right-hand panel. For a clear comparison, we marked some velocity components with dashed lines on these spectra. Seen from the multi-epoch spectra of the  $\text{H}_2\text{O}$  masers, the peak component was at  $\sim 62.8 \text{ km s}^{-1}$  on 2020 January 8,  $\sim 55.8 \text{ km s}^{-1}$  on March 20, and  $\sim 59.1 \text{ km s}^{-1}$  on March 31, April 1 and 7. In particular, the maser spectrum taken on March 20 was entirely different from those at other epochs. For example, there were some newly-detected maser components at  $\sim 73.5$ ,  $\sim 82.3$ , and  $\sim 92.5 \text{ km s}^{-1}$  on March 20; however, they disappeared at the last three epochs. This suggests that the physical conditions on March 20 should be different compared to other epochs. In Kim et al. (2019), the authors reported multiple epoch observations toward W51 for  $\text{H}_2\text{O}$  maser conducted on 2010 February 7, 2011 February 12, and 2017 June 19. However, no high  $\text{H}_2\text{O}$  maser variability such as the one that we detected in 2020 January–April was detectable in their observations (see Figure 1 in Kim et al. 2019 for comparison). This difference indicates that the mechanism for the  $\text{H}_2\text{O}$  maser variations might be different between our observations and those of Kim et al. (2019).

The locations of maser components at the above velocities provide clues to pinpoint the origin of the maser luminosity outburst. It can be seen from the lower right-hand panel of Figure 5 that most of the maser spots with strong variations during our monitoring mainly originated from W51 North in the sub-regions marked with “A,” “B,” and “C” (their corresponding velocity ranges are denoted in the maser spectra). By combining Figures 1, 5, and C1 in the Appendix, we found that the most luminous and variable maser spots are

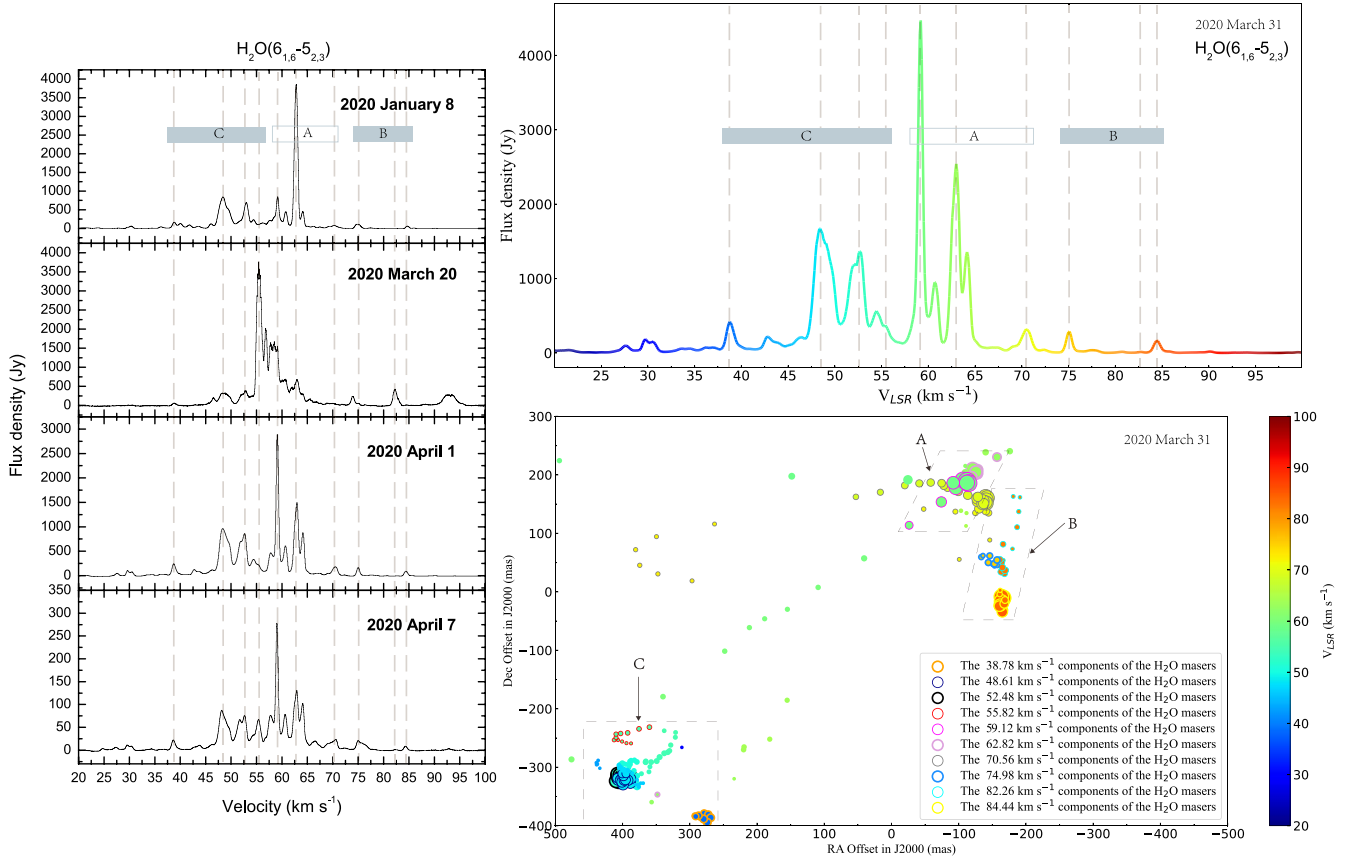


**Figure 5.** The left-hand panels present the spectra of the H<sub>2</sub>O maser detected in the four-epoch monitoring with TMRT during January to April 2020. Some velocity components with obvious variability are marked with dashed lines. The two right-hand panels give the spectrum and spatial distribution of the H<sub>2</sub>O masers detected with the VLA. For the maser spots at the marked velocities in the spectra, they are enclosed with circles in different colors in the maser distribution image in W51 North (lower right-hand panel). The reference position (offset = (0 mas, 0 mas)) in the J2000 coordinate is R.A. = 19<sup>h</sup>23<sup>m</sup>40<sup>s</sup>.047, decl. = +14<sup>°</sup>31′05″.530. The regions marked with “A,” “B,” and “C” show obvious maser variability from the multi-epoch monitoring with TMRT. Their corresponding velocity ranges are denoted in the maser spectra.

at the A region with velocities of  $\sim 59.1$  and  $\sim 62.8$  km s<sup>-1</sup>. In addition, the A region is likely to be distributed along with the edge of the disk. Interestingly, a jet-like structure from the A to C regions was newly detected in our VLA H<sub>2</sub>O maser observation, compared with the observations in Imai et al. (2002). In Figure 1, there is no continuum counterpart to be found around the C region. Seen from Figures 3 and 5, the locations of the regions A and B are likely to be correlated with the SiO and HC<sub>3</sub>N infalling streamer (see Section 3.3), while the region C is associated with the blue-shifted outflow. Based on these findings, the origin of the luminosity outburst and heatwave propagation detected in 2020 are likely to be involved with the A region.

It is reasonable to interpret the luminosity outburst from the perspective of the heatwave that caused by the energy release in the collision between the infall streamer and the disk in W51 North. On or even before 2020 January 8, the infalling streamer that fed mass onto the accretion disk or torus became an energy reservoir and was in an unsteady state. A dense clump (e.g., with a mass of  $0.25 M_{\odot}$ ; see below) in the infalling streamer collided or encountered the disk/torus at the A region (see Figure 5), which increased the temperature in the local environment until it was too high, and thus influenced the activity of the H<sub>2</sub>O maser, and even resulted in some components of the H<sub>2</sub>O maser emission (mainly the 62.8 km s<sup>-1</sup> component) located at that region being quenched. Then, the energy due to the collision was released and transmitted

outward from the A region, to wherever, including the inner disk of W51 North. The heatwave associated with the energy release first propagated in the B region, causing its H<sub>2</sub>O maser environment to be changed. Then, before March 20, the heatwave would have already propagated to the C region. Thus, the flux density of the 55.8 km s<sup>-1</sup> component located in the C region increased greatly. Before this time, the previous maser environments of all the A, B, and C regions were destroyed (e.g., gas/dust temperature increased owing to the heating by the heatwave), and thus quenched the masers from these regions. Meanwhile, some new maser components were excited, resulting in an entirely different maser spectrum detected on March 20 compared to the other epochs.

Considering the incline angle between the disk plane and the sky plane to be  $\sim 60^{\circ}$  (see Section 3.2), the spatial distance between the A and C regions was measured to be  $\sim 4850$  au, which is within the distance range (1000–5000 au) that we calculated for the heatwave propagating in the TMRT observations (Zhang et al. 2022). In Kobak et al. (2023) and Burns et al. (2020), the heatwave was calculated to propagate at 0.33 and 0.04–0.08 of the speed of light for another two luminosity burst sources, G24.33 + 0.14 and G358.930.03, respectively. The values obtained are lower than the speed of light, indicating that the maser variability may follow a thermal response time after being exposed to a wall of hot photons. Consequently, the heatwave’s speed will be significantly lower than that of light, particularly in an optically thick zone of dust



and gas. If we apply the former value (i.e., 0.33 of the speed of light) in our calculation, then the heatwave would spend  $\sim 85$  days for propagating from A to C regions, meaning that the time for the infalling clump hitting the disk was even before 2020 January 8, which is prior to the first observation epoch. The heatwave propagation should not be sheared from the rotating disk at the hitting location in the A region because it is related to photon radiative heating rather than kinematic process, which suggests that the heatwave could propagate directly from A to C regions. The 48.6 and 52.5 km s<sup>-1</sup> components in the C region were still stable during January 8 to March 20 compared to the other components, which supports the view that the heatwave originates from the A region and propagates from the A to C regions. This indicates that these two velocity components may be less affected by the heatwave compared to others, possibly due to the heatwave just arriving at the locations of the two maser components on March 20.

The previous maser excitation environment was re-established after the heatwave had passed away from the C region by March 31. Therefore, the maser spectra on March 31, and April 1 and 7 look like that on January 8, except that the flux density detected by TMRT dropped sharply ( $\sim 10$  times) from April 1 to 7. Considering the time separation of 7 days, an average decay rate of maser flux density of  $\sim 600$  Jy per day can be estimated. After the heatwave propagation, the strongest components were at  $\sim 59.1$  km s<sup>-1</sup>, rather than the previous 62.8 km s<sup>-1</sup>, and the  $\sim 82.3$  and  $\sim 92.5$  km s<sup>-1</sup> components that were enhanced on 2020 March 20 decreased and quenched, respectively.

Combining the previous works (e.g., Zapata et al. 2009, 2010) and our detection, a schematic view of the target is given in Appendix Figure C1. This figure shows that a high-mass protostar is actively forming with an infall accumulating mass from the envelope and feeding to the surrounding disk or torus in W51 North. If sometimes dense clumps infall onto the disk, then luminosity outbursts or even accretion bursts will happen and cause variations in the masers. While our data did not directly show an accreting clump in W51 North, Figures 1 and 3 reveal several scattering clumps in the infalling streamer. As a result, we can reasonably assume that the detected maser outburst was caused by the impact of dense clumps colliding with the disk. If we further assumed that the released energy is converted from kinetic energy of the dense clumps, then we can make a rough estimation for the energy to cause the luminosity outburst. Seen in Figure 4, the SiO infalling streamer would terminate at the disk with a LSR velocity  $\sim 80$  km s<sup>-1</sup>. This suggests that the actual net velocity would be  $\sim 40$  km s<sup>-1</sup>, considering the LSR systemic velocity of  $\sim 60$  km s<sup>-1</sup> and the incline angle of the infalling streamer along the LOS of 30° (see Section 3.3). Compared with Figure 2 in Tang et al. (2022), we found that the position of the 1.3 mm continuum object marked as ‘CB17’ is spatially consistent with the end of the infalling streamer onto the disk. The mass of ‘CB17’ was determined to be 0.25–0.30  $M_{\odot}$  in their paper. In Goddi et al. (2020), the infalling material in W51 North was estimated to be 0.25–0.50  $M_{\odot}$ . With the HC<sub>3</sub>N molecule assumed to be optically thin, we calculated the gas mass of the infalling HC<sub>3</sub>N clump (see Pineda et al. 2020; Chen et al. 2021) to be 0.82, 0.28, and 0.12  $M_{\odot}$  under temperatures of 14, 16, and 18 K, respectively (see Appendix Section D for details). Therefore, a moderate clump mass of 0.25  $M_{\odot}$  infalling to the disk/torus was assumed. We can then estimate the energy released by the

collision between the infall and the disk to be  $4.0 \times 10^{45}$  erg. This is comparable with the accretion energy in some known luminosity outburst sources, e.g.,  $3.2 \times 10^{46}$  erg for NGC6334I,  $1.2 \times 10^{46}$  erg for S255IR-NIRS3 and  $2.9 \times 10^{45}$  erg for G358.93-0.03 (Stecklum et al. 2021). Therefore, we infer that the luminosity outburst might be induced by the collision between the infalling streamer and the disk surrounding the protostar in W51 North.

Some other possibilities can account for the time variability of H<sub>2</sub>O masers detected in this work. Goddi et al. (2007) suggested that the high variability of the H<sub>2</sub>O maser emission could be caused by outflows or shocks passing through the emitting region. For example, changes of the orientation of the outflows (Goddi et al. 2020) would cause the time variability, but we did not find obvious difference in the location of the NW and SE maser clusters between Imai et al. (2002) and our VLA detection (see Figure 1). Meanwhile, the changes in the orientation of the disk/outflow system could not be as quick as months. Movements of random motions and shocks cannot cause rapid and strong bursts in our case, nor can they affect maser spots on such a vast scale, including the A, B, and C regions in Figure 5. In addition, as suggested in Chen et al. (2020b, 2020a), the disk fragmentation related to the accretion burst will also cause obvious maser time variability. Alternatively, the luminosity outburst and heatwave propagation may originate from the location wherein an accretion burst protostar resides. Nevertheless, we did not find the disk fragmentation by mapping the H<sub>2</sub>O maser spots (see Figures 1 and 5). Building a model is necessary to support our scenario that an infalling streamer hitting the disk would cause the heatwave propagation and maser variability, or to distinguish the above comparative possibilities. However, there is a lack of supportive and convincing material. In particular, our monitoring for the H<sub>2</sub>O maser was not intense enough to catch the details of this burst event in 2020, which limits our development of such a model. Therefore, an intense monitoring of a H<sub>2</sub>O maser with duration  $< 10$  days (Felli et al. 2007; Ladeyschikov et al. 2022) or other molecules is needed in the future.

## 5. Summary

We conducted a VLA observation on 2020 March 31 after detecting the luminosity outbursts in the H<sub>2</sub>O maser emission with TMRT toward W51-IRS2. We found a new ring-like structure traced by the H<sub>2</sub>O maser spots in the VLA data. By combining the ALMA data of C<sup>18</sup>O  $J=2-1$  and <sup>13</sup>CS  $J=5-4$  lines, we further confirmed the ring-like structure to be associated with the disk or torus surrounding the protostar in W51 North. A peculiar flow traced by the H<sub>2</sub>O maser, SiO  $J=5-4$  and HC<sub>3</sub>N  $J=24-23$  line emission was detected and confirmed to be an infall streamer, rather than an old outflow predicted by previous works. The energy release from the collision between the infalling streamer and disk/torus might account for the H<sub>2</sub>O maser luminosity outburst that happened in 2020. In addition to disk fragmentation induced by gravitational instability, this scheme may provide another mechanism for the luminosity outburst (or episodic accretion) that occurred during the high-mass star formation.

### Acknowledgments

This work is supported by the National Key R&D program of China (2022YFA1603102), the National Natural Science Foundation of China (11873002, 12011530065, 11590781). X. C. thanks Guangdong Province Universities and Colleges Pearl River Scholar Funded Scheme (2019). This work is also supported by the Great Bay Center, National Astronomical Data Center. This paper makes use of the following ALMA data: ADS/JAO.ALMA#2013.1.00308.S and 2015.1.01596.S.

### Appendix A

#### Keplerian Rotation Model for the C<sup>18</sup>O $J=2-1$ and <sup>13</sup>CS $J=5-4$ Lines

For a system undergoing Keplerian rotation, we followed the equation in Chen et al. (2021) to calculate the speed of rotation  $v(r)$  along the LOS:

$$\frac{v(r) - v_0}{\sin \theta} = \sqrt{\frac{GM}{r - r_0}}, \quad (\text{A1})$$

where  $v_0$  is the systemic velocity of the source,  $\theta$  is the inclination angle of the disk/torus rotational axis,  $G$  is the gravitational constants,  $M$  is the mass of the protostar system,  $r$  is the radius, and  $r_0$  is the reference offset on the P-V diagram. To obtain the incline angle between the disk (traced by the C<sup>18</sup>O  $J=2-1$  and <sup>13</sup>CS  $J=5-4$  transitions) and the sky plane, we utilized this Keplerian rotation model to fit the P-V diagrams of the two lines in Figure 2. For the C<sup>18</sup>O and <sup>13</sup>CS lines, the enclosed masses of the gravitational field are assumed to be 60 and 28  $M_\odot$ ,  $v_0$  is assumed to be 59.0 and 60.0 km s<sup>-1</sup>, respectively, and  $r_0$  is assumed to be the same 1''1. We can then determine the incline angle to be 20°.

### Appendix B

#### The Kinematic Model for the Gravitationally Controlled Infalling Streamer

To further study the property of the SiO infalling streamer, we followed the equation in Chen et al. (2021) to fit the infalling streamer under gravitationally controlled kinematics:

$$\frac{v(r) - v_0}{\cos \theta} = \sqrt{\frac{2GM}{r - r_0}}, \quad (\text{B1})$$

where  $v_0$  is the velocity at the starting position of the streamer,  $\theta$  is the incline angle of the streamer along the LOS, and  $r_0$  is the projection height of the landing point of the streamer onto the disk/torus. Since the infalling streamer extends far beyond the H<sub>2</sub>O maser map (see Figure 1), it requires more mass to gravitationally control the infalling. Therefore, we assumed the total mass  $M$  of the gravitational field to be  $\sim 60 M_\odot$  (Zapata et al. 2009), we then obtained the incline angle of the infalling streamer along the LOS in the best fitting result to be  $\sim 30^\circ$ .

### Appendix C

#### The 2D Model and the Cartoon for Illustrating the Structure of the Target

The newly-detected H<sub>2</sub>O maser spots in our VLA observation suggest a rotation ring-like structure surrounding the central protostar, which likely traces a disk or torus. To test this speculation, we followed the model in Chen et al. (2020a) to fit the ring-like distribution of the maser spots presented in Figure 1. The equation is:

$$v_{\text{LSR}(x,y)} = \sqrt{\frac{GM}{r}} \cos \phi \sin \theta, \quad (\text{C1})$$



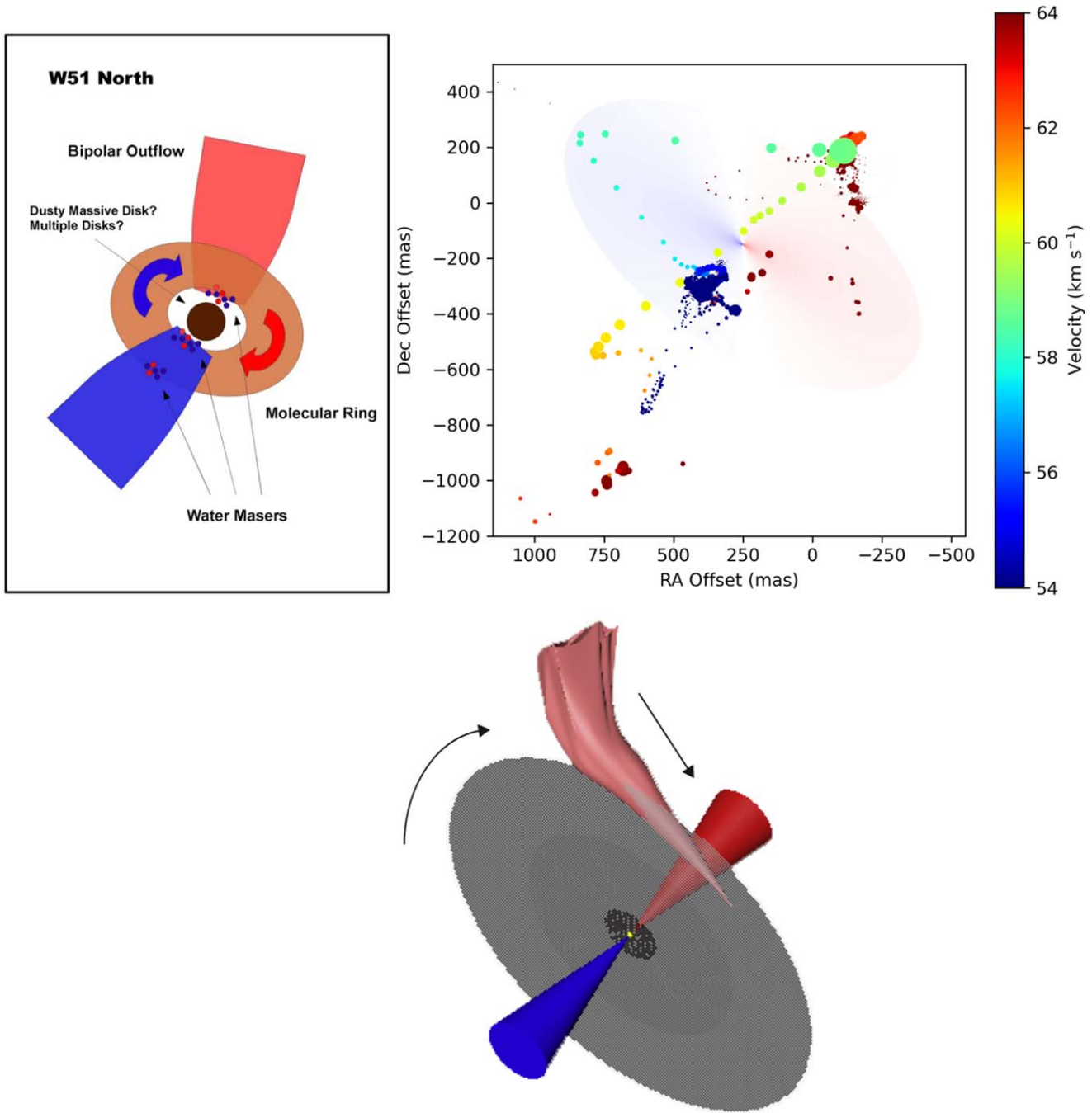


**Figure C1.** Upper left-hand panel: the artist’s conception for the overview structures of W51N, which are extracted from Zapata et al. (2009). Upper right-hand panel: the zoomed-in view of the H<sub>2</sub>O maser spots in the velocity range of 54~64 km s<sup>-1</sup> detected with our VLA observation overlaid on the radial velocity field of the disk projected onto the sky plane. The reference position (offset = (0 mas, 0 mas)) in J2000 coordinate is R.A. = 19<sup>h</sup>23<sup>m</sup>40<sup>s</sup>.047, decl. = +14°31′05″.530. Lower panel: a cartoon front view of the kinematic features of W51 North. The infalling streamer is shown in light-red. The modeled disk is shown in gray with different transparencies, which indicate the inner and outer portions of the disk. The rotational and infalling orientations are shown with arrows near to the infalling streamer and the disk, respectively.

where  $\phi$  is the azimuthal angle in the disk/torus plane with the origin ( $\phi = 0$ ) setting to be along the crossing line between the disk/torus plane and the sky plane, as shown in Appendix Figure C1. The coordinates  $(x,y)$  are the positions on the sky plane, which can be converted through  $x = r \sin \phi \cos \theta$  and  $y = r \cos \phi$ . To obtain the radius and the incline angle of the disk/torus plane indicated by the maser spots relative to the sky plane, we carried out a fitting to the ring-like distributed H<sub>2</sub>O

maser spots and present it in the left-hand panel of Appendix Figure C1. It is found that the outer radius of the disk traced by the masers is about 4000 au and the incline angle is about 60°.

In addition, a cartoon will be a helpful tool to illustrate the content and clarify the structure. For this purpose, we present a simple cartoon for the overall structure of the source (including the Keplerian disk, outflow, and infalling streamer) in the right-hand panel of Appendix Figure C1.

## Appendix D The Mass and Energy Release of the Infalling Clump Hitting the Disk

Using the chemically fresh molecule  $\text{HC}_3\text{N}$ , we can roughly determine the mass of the clump that hits the disk. Assuming the infalling streamer to be optically thin in  $\text{HC}_3\text{N}$ , the column density of this molecule can be calculated using the formula (Blake et al. 1987; Chen et al. 2013, 2021):

$$N = \frac{3\kappa_B W'}{8\pi^3 \mu S \nu^2} \frac{T_{\text{ex}}}{T_{\text{ex}} - T_{\text{bg}}} Q_{T_{\text{ex}}} e^{-\frac{E_u}{\kappa_B T_{\text{ex}}}} \quad (\text{D1})$$

where  $\kappa_B$  is the Boltzmann constant in  $\text{erg K}^{-1}$ ,  $W'$  is the observed integrated intensity of the line profile in units of  $\text{K km s}^{-1}$ ,  $S\nu^2$  is the product of the total torsion-rotational line strength and the square of the electric dipole moment,  $T_{\text{ex}}$  and  $T_{\text{bg}}$  are the excitation temperature and the 2.73 K background temperature, respectively,  $Q_{T_{\text{ex}}}$  is the partition function at temperature  $T_{\text{ex}}$ , and  $\frac{E_u}{\kappa_B}$  is the upper-level energy in K.

To calculate the mass of the infalling clump, one needs to obtain the total column density of the hydrogen elements. In He et al. (2021), the mean abundance of  $\text{HC}_3\text{N}$  ( $X_{\text{HC}_3\text{N}} = N_{\text{HC}_3\text{N}}/N_{\text{tot}}$ ) was determined to be  $1.14 \times 10^{-9}$  from 43 massive star-forming regions. With this value used in the following formula (Chen et al. 2021), we can determine the mass of the clump,

$$M_c = \int \mu m_{\text{H}} N_{\text{tot}} dA \quad (\text{D2})$$

where  $\mu = 2.33$  (Myers & Benson 1983; Chen et al. 2021),  $m_{\text{H}}$ , and  $A$  are the mean molecular weight, mass of the hydrogen atom, and area of the infalling streamer, respectively.

The integrated intensity of the line profile in the chemically fresh molecule  $\text{HC}_3\text{N}$  and the ALMA beam in 1.3 mm are  $472.73 \pm 16.21 \text{ K km s}^{-1}$  and  $2.73 \times 10^{-3} \text{ arcsec}^2$ . By assuming that the infalling clump has the same scale as the beam size, we then obtained that the masses of the clump will be 0.82, 0.28, and  $0.12 M_{\odot}$  under the excitation temperatures of 14, 16, and 18 K, respectively.

In comparison with values of infalling mass in W51 North reported in the literature, such as 0.25–0.30  $M_{\odot}$  in Tang et al. (2022) and 0.25–0.50  $M_{\odot}$  in Goddi et al. (2020), we estimated the infalling clump's mass to be 0.25  $M_{\odot}$ . We utilized the following formula to calculate the energy released upon impact,

$$E = \frac{1}{2} m \left( \frac{\Delta v}{\sin \theta} \right)^2 \quad (\text{D3})$$


where  $E$ ,  $m$ ,  $\Delta v$ , and  $\theta$  are the released energy, the mass of the infalling clump, the end velocity of the freefall motion and the incline angle of the streamer along the LOS, respectively. In Figure 4 and the calculation in Appendix B, we got

$\Delta v \sim 20 \text{ km s}^{-1}$  and  $\theta \sim 30^\circ$ , and then  $E$  was calculated to be  $4.0 \times 10^{45} \text{ erg}$ .

## ORCID iDs

Yan-Kun Zhang  <https://orcid.org/0000-0001-7817-1975>

Xi Chen  <https://orcid.org/0000-0002-5435-925X>

Shi-Ming Song  <https://orcid.org/0000-0003-3640-3875>

You-Xin Wang  <https://orcid.org/0000-0001-9155-0777>

## References

- Blake, G. A., Sutton, E. C., Masson, C. R., & Phillips, T. G. 1987, *ApJ*, 315, 621
- Brogan, C. L., Hunter, T. R., Townner, A. P. M., et al. 2019, *ApJL*, 881, L39
- Burns, R. A., Sugiyama, K., Hirota, T., et al. 2020, *NatAs*, 4, 506
- Caratti o Garatti, A., Stecklum, B., Garcia Lopez, R., et al. 2017, *NatPh*, 13, 276
- Chen, X., Gan, C.-G., Ellingsen, S. P., et al. 2013, *ApJS*, 206, 9
- Chen, X., Ren, Z.-Y., Li, D.-L., et al. 2021, *ApJL*, 923, L20
- Chen, X., Sobolev, A. M., Breen, S. L., et al. 2020a, *ApJL*, 890, L22
- Chen, X., Sobolev, A. M., Ren, Z.-Y., et al. 2020b, *NatAs*, 4, 1170
- Felli, M., Brand, J., Cesaroni, R., et al. 2007, *A&A*, 476, 373
- Ginsburg, A., Goddi, C., Kruijssen, J. M. D., et al. 2017, *ApJ*, 842, 92
- Goddi, C., Ginsburg, A., Maud, L. T., Zhang, Q., & Zapata, L. A. 2020, *ApJ*, 905, 25
- Goddi, C., Moscadelli, L., Sanna, A., Cesaroni, R., & Minier, V. 2007, *A&A*, 461, 1027
- He, Y.-X., Henkel, C., Zhou, J.-J., et al. 2021, *ApJS*, 253, 2
- Herbig, G. H. 1977, *ApJ*, 217, 693
- Herbig, G. H. 1989, ESO Workshop on Low Mass Star Formation and Pre-Main Sequence Objects (München: European Southern Observatory), 233
- Hirota, T., Wolak, P., Hunter, T. R., et al. 2022, *PASJ*, 74, 1234
- Hunter, T. R., Brogan, C. L., De Buizer, J. M., et al. 2021, *ApJL*, 912, L17
- Hunter, T. R., Brogan, C. L., MacLeod, G., et al. 2017, *ApJL*, 837, L29
- Imai, H., Watanabe, T., Omodaka, T., et al. 2002, *PASJ*, 54, 741
- Kenyon, S. J., Hartmann, L. W., Strom, K. M., & Strom, S. E. 1990, *AJ*, 99, 869
- Kim, W.-J., Kim, K.-T., & Kim, K.-T. 2019, *ApJS*, 244, 2
- Kobak, A., Bartkiewicz, A., Szymczak, M., et al. 2023, *A&A*, 671, A135
- Ladeyschikov, D. A., Gong, Y., Sobolev, A. M., et al. 2022, *ApJS*, 261, 14
- MacLeod, G. C., Smits, D. P., Goedhart, S., et al. 2018, *MNRAS*, 478, 1077
- MacLeod, G. C., Sugiyama, K., Hunter, T. R., et al. 2019, *MNRAS*, 489, 3981
- Meyer, D. M. A., Haemmerlé, L., & Vorobyov, E. I. 2019, *MNRAS*, 484, 2482
- Meyer, D. M. A., Vorobyov, E. I., Elbakyan, V. G., et al. 2021, *MNRAS*, 500, 4448
- Miao, D., Chen, X., Song, S.-M., et al. 2022, *ApJS*, 263, 9
- Myers, P. C., & Benson, P. J. 1983, *ApJ*, 266, 309
- Oliva, G. A., & Kuiper, R. 2020, *A&A*, 644, A41
- Pineda, J. E., Segura-Cox, D., Caselli, P., et al. 2020, *NatAs*, 4, 1158
- Semkov, E., Ibryamov, S., & Peneva, S. 2021, *Symm*, 13, 2433
- Sollins, P. K., Zhang, Q., & Ho, P. T. P. 2004, *ApJ*, 606, 943
- Stecklum, B., Caratti o Garatti, A., Cardenas, M. C., et al. 2016, *ATel*, 8732, 1
- Stecklum, B., Wolf, V., Linz, H., et al. 2021, *A&A*, 646, A161
- Tang, M., Palau, A., Zapata, L. A., & Qin, S.-L. 2022, *A&A*, 657, A30
- Valdivia-Mena, M. T., Pineda, J. E., Segura-Cox, D. M., et al. 2022, *A&A*, 667, A12
- Xu, Y., Reid, M. J., Menten, K. M., et al. 2009, *ApJ*, 693, 413
- Zapata, L. A., Ho, P. T. P., Schilke, P., et al. 2009, *ApJ*, 698, 1422
- Zapata, L. A., Palau, A., Ho, P. T. P., et al. 2008, *A&A*, 479, L25
- Zapata, L. A., Tang, Y.-W., & Leurini, S. 2010, *ApJ*, 725, 1091
- Zhang, Y.-K., Chen, X., Sobolev, A. M., et al. 2022, *ApJS*, 260, 34